Journal of Colloid and Interface Science 509 (2018) 219–234

Contents lists available at ScienceDirect

Journal of Colloid and Interface Science

journal homepage: www.elsevier.com/locate/jcis

Facile fabrication of mediator-free Z-scheme photocatalyst of phosphorous-doped ultrathin graphitic carbon nitride nanosheets and bismuth vanadate composites with enhanced tetracycline degradation under visible light

Yaocheng Deng[a,b], Lin Tang[a,b,*], Guangming Zeng[a,b,*], Jiajia Wang[a,b], Yaoyu Zhou[c], Jingjing Wang[a,b], Jing Tang[a,b], Longlu Wang[d], Chengyang Feng[a,b]

[a] College of Environmental Science and Engineering, Hunan University, Changsha 410082, China
[b] Key Laboratory of Environmental Biology and Pollution Control, Hunan University, Ministry of Education, Changsha 410082, China
[c] College of Resources and Environment, Hunan Agricultural University, Changsha 410128, China
[d] State Key Laboratory of Chemo/Biosensing and Chemometrics, Hunan University, Changsha 410082, PR China

GRAPHICAL ABSTRACT

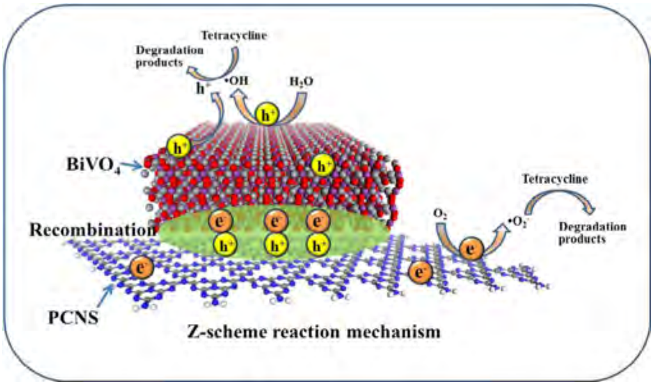

ARTICLE INFO

Article history:
Received 16 June 2017
Revised 9 August 2017
Accepted 5 September 2017
Available online 07 September 2017

Keywords:
Tetracycline
Z-scheme photocatalyst
Phosphorous-doped g-C_3N_4
$BiVO_4$
Visible light response

ABSTRACT

To realize the sustainable employment of solar energy in contaminant degradation and environmental recovery, design and development of an efficient photocatalyst is urgently needed. Herein, a novel direct Z-scheme composite photocatalysts consist of phosphorous-doped ultrathin g-C_3N_4 nanosheets (PCNS) and bismuth vanadate ($BiVO_4$) are developed via a one-pot impregnated precipitation method. The as-prepared hybrid nanocomposite was utilized for the degradation tetracycline (TC) under visible light irradiation. Among the composites with various PCNS/$BiVO_4$ ratios, the prepared PCNS/BVO-400 photocatalyst presents the best performance, showing a TC (10 mg/L) removal efficiency of 96.95% within 60 min, more than double that of pristine $BiVO_4$ (41.45%) and higher than that of pure PCNS (71.78%) under the same conditions. The effects of initial TC concentration, catalyst dosage, pH value and different water sources have been studied in detail. The improved photocatalytic performance of the as-prepared PCNS/$BiVO_4$ nanocomposites could be attributed to the promoted separation efficiency of the photogenerated electrons and the enhanced charge carrier lifetime (1.65 ns) owing to the synergistic effect between the PCNS and $BiVO_4$. The degradation intermediates and decomposition pathway of TC were also

---

* Corresponding authors at: College of Environmental Science and Engineering, Hunan University, Changsha 410082, China.
E-mail addresses: tanglin@hnu.edu.cn (L. Tang), zgming@hnu.edu.cn (G. Zeng).

http://dx.doi.org/10.1016/j.jcis.2017.09.016

analyzed and proposed. Additionally, radical trapping experiments and ESR measurement indicated that the photogenerated holes (h^+), superoxide radical ($\cdot O_2^-$) and hydroxyl radical ($\cdot OH$) all participated in the TC removal procedure in the reaction system. The high performance of PCNS/BVO-400 in real wastewater indicated the potential of the prepared composite in practical application. This work provides an efficient and promising approach for the formation of high performance Z-scheme photocatalyst and study the possibility for real wastewater treatment.

1. Introduction

Antibiotics have been widely employed to help human and animals fight for diseases. Tetracycline (TC), as one of the extensively used antibiotic in the world, plays great role on the field of both human therapy and animal husbandry owing to its broad-spectrum antimicrobial ability against various diseases [1–5]. However, owing to the essential characteristics of antibiotics, TC can only be partial metabolized by humans and animals, which causes the large release of the residues into wastewater [6–8]. Besides, traditional wastewater treatment cannot remove TC from aqueous solution efficiently due to its chemical stability and antibacterial nature. The released TC tends to accumulate in the environment and poses serious threat to human health and ecosystem by developing antibiotic resistant bacteria or pathogens [9–12]. Therefore, how to effectively eliminate TC from environment has become a necessary and urgent public issue.

Recently, many treatment methods have been employed for TC removal, such as adsorption, ozone oxidation, Fenton-like system and photocatalysis [13–15]. Among these methods, photocatalytic degradation of TC based on semiconductor reaction system is regarded as an efficient approach and has attracted great attentions [16–18]. Photocatalytic degradation of TC can be achieved based on the existence of photocatalysts under relative mild reaction conditions, some other advantages such as low toxicity, low cost, high degradation activity and complete mineralization ability are also included. As is known to all, the photocatalytic decomposition efficiency is greatly depended on the photocatalysts. However, the most widely studied and used photocatalyst is TiO_2, its employment is severely limited due to its wide band gap, which means that it can only be excited by ultraviolet light. Additionally, the fast recombination rate of photogenerated charges in TiO_2 also inhibits its photocatalytic activity greatly [19–22]. To overcome the drawbacks of TiO_2 based nanocomposites, many novel visible light response photocatalysts with high photocatalytic activity have been develop [23–29]. Among these new photocatalysts, bismuth-based photocatalysts are regarded as good candidates owing to the interaction between 2p O and 6s Bi orbital at the top of the valence band, and its potential visible light response ability [24]. Especially for monoclinic bismuth vanadate (m-$BiVO_4$), owing to its suitable bandgap (around 2.4 eV), excellent chemical stability and energy conversion, has attracted great attentions [30–33]. However, as for pristine $BiVO_4$, the relative photocatalytic activity still needs to be improved, because its weak transportation ability of photogenerated electrons and limited specific surface area for reaction targets adsorption hinder its photocatalytic performance greatly [34]. In the past decades, the couple of two or more semiconductors for the design of heterostructure photocatalytic system has been regarded an efficient method to overcome the problems that existed in single component reaction system and to acquire high photocatalytic performance [25,35,36]. But an unavoidable obstacle for traditional heterojunction is the reduced redox ability of the photogenerated charges due to the migration process [37], which means that it is difficult to realize the simultaneous acquisition of high photogenerated charge separation efficiency and strong redox ability. To solve this problem, Z-scheme photocatalytic reaction system has been put forwards and emphasized, and has been widely discussed for its ability in not only accelerating the migration of the photogenerated charges, but also keeping its strong ability without the transfer process [34]. In previous study, graphene was used as the bridged and electron mediator to form the Z-scheme $Ag_3PO_4/Ag/BiVO_4$ photocatalyst and present enhanced photocatalytic performance [38]. However, most of the Z-scheme reaction system based on two different semiconductors combined with an appropriate electron mediators, such as Au, Ag, Fe^{3+}/Fe^{2+}, IO^{3-}/I^- and graphene [38–42], which results in the difficulties for realistic application due to the complex reaction system. Therefore, to simplify the reaction system and achieve the same effect, the construction of direct Z-scheme photocatalysts without the need of mediator will be the most the promising candidate for realistic application.

Recently, graphite-like carbon nitride (g-C_3N_4) has attracted great attentions and been widely employed in photodegradation and hydrogen production field owing to its low coat, easy to prepared, excellent chemical stability and narrow band gap for visible light response [27,43–46]. However, due to the inherent defect of single component, the photocatalytic performance of pure g-C_3N_4 is unsatisfactory owing to the limited transfer rate of the photogenerated charges and relative low specific surface area. Strategies such as the constructed hybrid nanocomposites and the surface morphology adjustments have been demonstrated are efficient for promoting its photocatalytic performance [29,35,47–50]. In our group, Ag_2CrO_4/g-C_3N_4 Z-scheme has been synthesized and presents enhanced photocatalytic degradation activity towards dye pollutants [23]. We also prepared phosphorous-doped porous ultrathin g-C_3N_4 nanosheets and investigated its enhanced photocatalytic performance for simultaneous photocatalytic removal of Cr(VI) and 2,4-diclorphenol under visible light irradiation [51]. And we found that the prepared phosphorous-doped ultrathin g-C_3N_4 nanosheets show wide visible light absorption ability and fast transfer capacity of the photogenerated electrons and holes. Besides, considering that the suitable band structure of g-C_3N_4 and $BiVO_4$, the excited electrons produced in the conduction band of $BiVO_4$ tends to combine with the holes generated in the valence band of g-C_3N_4, which prefer to the formation of direct Z-scheme reaction process. So the combination of phosphorus doped ultrathin g-C_3N_4 nanosheets and $BiVO_4$ would present high photocatalytic activity, and the systematical study of its photodegradation activity towards TC removal will be favorable to understand its direct Z-scheme reaction mechanism.

In this work, a novel redox-mediator-free direct Z-scheme composite photocatalyst of phosphorus doped ultrathin g-C_3N_4 nanosheets/$BiVO_4$ (PCNS/BVO) is developed and applied for effective TC removal. To increase the efficiency, the band gap of g-C_3N_4 can be adjusted by phosphorus doping, and the relative specific surface area can be increased due to the formation of ultrathin g-C_3N_4 nanosheets. A composite photocatalyst with PCNS and $BiVO_4$ was simply synthesized via impregnated co-precipitation method. The improved photocatalytic performance of the prepared hybrid nanocomposites for the degradation of TC should be attributed to the synergistic effect between PCNS and $BiVO_4$. As for realistic applications, the influence of different reaction conditions such as photocatalyst dosage, initial TC concentrations, pH values and different water sources has been investigated in detail. The degradation intermediates and decomposition pathway of TC also have been analyzed and proposed. The obtained results show that the prepared PCNS/BVO photocatalyst presents excellent performance for the degradation of TC contaminant both in deionized water and real wastewater. A direct Z-scheme reaction mechanism was proposed to better understand the reaction process based on PCNS/BVO hybrid nanocomposites.

2. Experimental section

2.1. Materials

2-Aminoethylphosphonic acid (AEP) (>99%) was purchased from Sigma-Aldrich (USA). Melamine, bismuth nitrate pentahydrate ($Bi(NO_3)_3{\cdot}5H_2O$), ammonium metavanadate (NH_4VO_3), urea, tetracycline were purchased from Sinopharm Chemical Reagent Co. Ltd (Shanghai, China). All reagents were used as received from commercial suppliers without further purification. Deionized water (18.25 MΩ cm specific resistance) generated by an Ultrapure laboratory water system was used to prepare all solutions.

2.2. Preparation of PCNS

Phosphorus doped ultrathin $g\text{-}C_3N_4$ nanosheets (PCNS) were synthesized according to the previous report with some modifications [51,52]. Typically, AEP and melamine were dissolved thoroughly in deionized water with a weight ratio of 1:60, and heated to 80 °C to completely evaporate the solvent and acquire the crystal complex. Then, the crystal complex was milled into powder and placed in a quartz container with a cover, and heated from room temperature to 500 °C and kept for 3 h under N_2 ambient. Subsequently, the temperature was further increased to 550 °C and kept at this temperature for another 5 h. Then the brown agglomerates were obtained and ground into powder. Finally, the PCNS can be obtained by further thermal exfoliating the brown powder to 500 °C for another 2 h under static air condition. To make comparison, pristine $g\text{-}C_3N_4$ nanosheets (CNS) were also prepared according to the process mentioned above without the addition of AEP.

2.3. Preparation of PCNS/$BiVO_4$

Pristine $BiVO_4$ was synthesized by a reported procedure [53]. 12.0 mmol of bismuth nitrate pentahydrate and 12.0 mmol of ammonium metavanadate were separately dissolved in 50 mL of a 2.0 M nitric acid solution. Then two solutions were mixed slowly and formed a yellow homogeneous solution. Subsequently, 5.0 g of urea was added into the above solution and stirred at 90 °C in oil bath for 24 h. Due to the hydrolysis of urea, the increasing pH of the solution can help the crystallization process of $BiVO_4$. Finally, the precipitate was filtered, washed with ethanol and water for several times and dried. In order to synthesize PCNS/$BiVO_4$ composite, certain amount of PCNS powder was placed and impregnated in 10 mL of the above mentioned yellow $BiVO_4$ homogeneous precursor solution and kept stirring for 1 h. Then, 0.5 g of urea was added and kept stirring at 90 °C for 24 h. and the prepared samples was filtered, washed and dried. The prepared samples were marked as PCNS/BVO-X (X represent the added weight of PCNS in the preparation process). For comparison, the mechanical mixing of 387 mg of $BiVO_4$ and 400 mg PCNS was also prepared, labeled as Mechanical Mixed. All synthesized photocatalysts were well-ground by an agate mortar and sieved. The prepared procedure of PCNS/BVO was illustrated in Scheme 1.

2.4. Characterizations

The crystal properties of the as-prepared samples were investigated by using an X-ray diffractometer (XRD) (Bruker AXS D8 Advances) with Cu Kα irradiation source at a scan rate (2θ) of $0.05°\ s^{-1}$. Morphological measurement was obtained using a Hitachi S-4800 field emission scanning electron microscopy (FE-SEM Hitachi, Japan) with 5.0 kV scanning voltages. Transmission electron microscopy (TEM) images were obtained on an F20 S-TWIN electron microscopy (Tecnai G2, FEI Co.) at the acceleration voltage

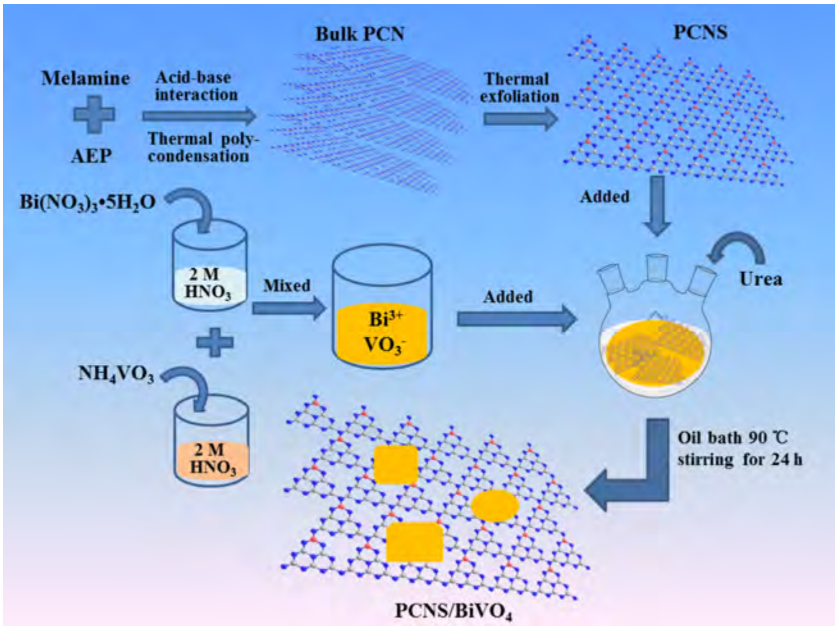

Scheme 1. Schematic diagram of the preparation process of phosphorous-doped ultrathin $g\text{-}C_3N_4$ nanosheets/$BiVO_4$ nanocomposites.

of 200 kV. FT-IR spectra were collected on an IRAffinity-1 Fourier transform infrared spectrometer (Shimadzu, Japan) at room temperature by the standard KBr disk method. The X-ray photoelectron spectroscopy of the prepared samples was carried out Thermo Fisher ESCALAB 250Xi spectrometer with Al Kα source. The specific surface areas of the prepared samples were characterized via a nitrogen adsorption-desorption and Brunauer-Emmett-Teller (BET) method by a surface area analyzer (NOVA 2200e, Quantachrome). The Ultraviolet visible diffused reflectance spectra (UV–vis DRS) of the prepared samples were carried out via a UV–vis spectrophotometer (Cary 300, USA) equipped with an integrating sphere, using $BaSO_4$ as the reference. The zeta potentials of the samples were evaluated as a function of pH (adjusted by 0.1 M HNO_3 or NaOH) using a Zeta-sizer Nano-ZS (Malvern). The total organic carbon (TOC) assays were measured using a Shimadzu TOC-VCPH analyzer. The electron spin resonance (ESR) signals of radicals spin-trapped by spin-trapped reagent 5,5-dimethyl-l-pyrroline N-oxide (DMPO) were examined on a Bruker ER200-SRC spectrometer under visible light irradiation ($\lambda > 420$ nm).

2.5. Evaluation of photocatalytic activity

The photocatalytic performances of the prepared samples were measured by photodegrading TC under visible light irradiation. A 300 W Xe lamp (PLS-SXE 300 C, Beijing Perfectlight Co., Ltd.) equipped with a UV cut of filter ($\lambda > 420$ nm) was used as the visible light source. Before irradiation start, 100 mg photocatalysts was dispersed in a 100 mL 10 mg/L TC aqueous solution, and the suspension was stirred in the dark for 30 min to ensure the adsorption-desorption equilibrium between the photocatalyst and TC. During the illumination process, 3 mL of reaction solution was collected and labeled at certain time intervals, and subsequently centrifuged and filtered through Millipore filter to remove the residual photocatalysts. The concentration of TC was measured by a Shimadzu UV–vis spectrophotometer (UV-2550) with the characteristic absorbance peak of 357 nm.

2.6. Liquid chromatography–mass spectrometry

Reaction products of TC were identified using liquid chromatography with tandem mass spectrometry (HPLC-MS/MS), consisting of an Aglient 1290 series HPLC coupled to a G6460 triple quadrupole mass spectrometer (Agilent Technologies, USA). Separation was accomplished using an Aglient Kromasil C18 column (4.6 × 100 mm). Elution was performed at a flow rate of 0.3 mL min^{-1} with H_2O containing 0.1% (v/v) formic acid as eluent A and methanol containing 0.1% (v/v) formic acid as eluent B. The separation of the analytes was achieved by a mixture solution with eluent A and B (5% A, 95% B), injected volume of 10 μL, and column temperature at 307 K (35 °C). Mass spectra analysis was conducted in positive mode using an electrospray ionization (ESI) source, and mass analyzer was operated in full scan mode (m/z range 200–600) to identify the products. Instrument parameters were set as follows: capillary voltage 4.0 kV, the desolvation gas was N_2 with the flow rate of 10 L min^{-1}, temperature 350 °C, nebulizer pressure 15 psi, nitrogen was used as a collision gas at 0.25 MPa.

2.7. Photoelectrochemical measurement

To further study the photoelectrochemical characteristics of the prepared samples, the photocurrent response, cathodic polarization curves and electrochemical impedance spectroscopy (EIS) were measured. The photocurrent density were carried out on a CHI 660D workstation in a three-electrode model. A Pt electrode was used as the counter electrode and an Ag/AgCl electrode in saturated KCl solution was employed as the reference electrode. The photocatalysts were coating on the FTO as the working electrode. Typically, the working electrodes were prepared as follows. 10 mg of the photocatalyst was suspended in 1 mL 0.5% Nafion solution to make slurry. Then, 100 μL of the slurry dropped onto a 1 cm × 2 cm FTO slice with an effective working area of 1 cm^2. The photoelectrochemical test system was conducted in a 0.2 M sodium sulfate electrolyte solution under visible light provided by a 300 Xe arc lamp. The cathodic polarization curves were obtained using the linear sweep voltammetry (LSV) technique with a scan rate of 0.2 mV s^{-1}. The electrochemical impedance spectroscopy (EIS) was performed on an Autolab workstation (AUT85812) equipped with a frequency analyzer module based on the above three-electrode system in 0.2 M Na_2SO_4.

2.8. Active species trapping experiments

To determine the active species in the photocatalytic process, some sacrificial agents, such ethylenediamintetraacetic acid disodium (EDTA-Na_2), 2-propanol (IPA), and 1,4-benzoquinone (BQ) were used as the hole (h^+) scavenge, hydroxyl radical ($\cdot OH$) scavenger, and superoxide radical ($\cdot O_2^-$) scavenge, respectively. The method was similar to the former photocatalytic activity test with the addition of 1 mM of scavenger in the presence of TC.

3. Result and discussion

3.1. Structure and morphology characteristics

The crystalline structure of the prepared samples was investigated by XRD analysis. As shown in Fig. 1, the XRD patterns of pure PCNS, pure $BiVO_4$ and PCNS/BVO nanocomposites with different mass ratios are provided. For the pure PCNS, two distinct diffraction peaks locate at 27.3° and 13.4° can be observed, referring to the (0 0 2) and (1 0 0) diffraction planes, respectively, which indicate the prepared PCNS owns the crystal structure of tetragonal phase of $g\text{-}C_3N_4$ (JCPDS 50-1250) [52]. As for pure $BiVO_4$, its XRD pattern owns a series of sharp and narrow diffraction peaks, corresponding to the monoclinic phase of $BiVO_4$ (JCPDS 14-0688) [54]. For the XRD patterns of PCNS/$BiVO_4$ samples, the main peaks observed in that of pure $BiVO_4$ exist in all the PCNS/$BiVO_4$ samples. However, the (0 0 2) characteristic diffraction plane of PCNS also included in these samples and gradually rises with the increased

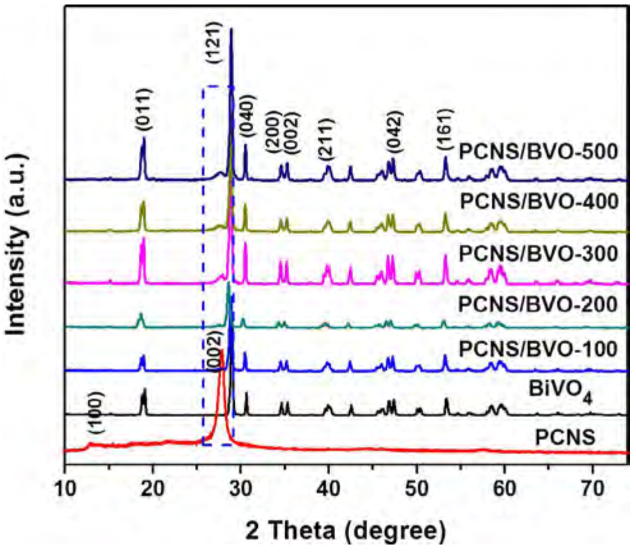

Fig. 1. XRD patterns of the prepared samples.

PCNS content. The XRD results of the samples indicate the co-existence of characteristic diffraction peaks of both PCNS and $BiVO_4$ component in the prepared PCNS/$BiVO_4$ samples.

The morphology of PCNS, $BiVO_4$ and PCNS/BVO-400 were investigated by SEM and the images are shown in Fig. 2. From Fig. 2a and b, we can see that the prepared pure PCNS presenting nanosheets structure and consisting of several stacking layers, in agreement with the results shown in other publications [52,55,56]. The pure $BiVO_4$ sample presents block-shaped particles with a size of 0.5–3 μm and owns smooth surface (Fig. 2c and d). As for the prepared PCNS/BVO-400 sample, its morphology presents some differences compared with that of pure PCNS and pure $BiVO_4$. As shown in Fig. 2e and f, the prepared PCNS/BVO-400 discloses clustered structure, indicating the intimate contact of PCNS and $BiVO_4$ particles. Additionally, due to the existence of PCNS, the particle size of $BiVO_4$ particles in PCNS/BVO-400 nanocomposites are much smaller than pure $BiVO_4$, which indicate that the PCNS can be used as the substrate for the formation of $BiVO_4$ and can provide more reaction sites than pure $BiVO_4$.

More detailed morphology of the prepared PCNS/BVO-400 was further demonstrated by TEM analysis (Fig. 3a and b). The TEM image of PCNS/BVO-400 displays that two materials with discriminative morphologies are adhere together. One with the semitransparent structure refers to the prepared PCNS, and the other one presents an opaque structure can be identified as $BiVO_4$ particles. HR-TEM image in Fig. 3c shows two distinguished parts in the nanocomposites. One part owns the crystal structure with the lattice spacing of 0.259 nm, which belongs to the 200 plane of $BiVO_4$. Another amorphous part refers to the prepared PCNS sample. The results demonstrated the co-existence of both PCNS and $BiVO_4$, and their intimate connection with each other, which is important for their high photocatalytic performance in the following photocatalytic experiments. Additionally, the EDS mapping of the red box area marked in Fig. 3d further demonstrate the presence of C, N, P, O, V and Bi elements in the PCNS/BVO-400 nanocomposites, which strongly demonstrate the successful preparation of PCNS/BVO hybrid nanocomposites.

3.2. Specific surface areas analysis

To measure and analyze the specific surface areas of the prepared samples, N_2 adsorption-desorption isotherms of PCNS, $BiVO_4$ and PCNS/BVO-400 nanocomposite are provided in Fig. 4. Based on the principles shown in the IUPAC Brunauer-Emmett-Teller classification, the prepared PCNS and PCNS/BVO-400 nanocomposites display a type IV of N_2 adsorption-desorption isotherms and an H3-type hysteresis loop ($P/P_0 > 0.4$), thus indicating the existence of pore structure. The specific surface areas and pore volumes of the prepared samples are shown in the inset table. The specific surface areas of the prepared PCNS, $BiVO_4$ and PCNS/BVO-400 nanocomposites are calculated to be 102.5, 2.1 and 24.6 m^2/g, respectively. And the relative pore volumes of these three samples

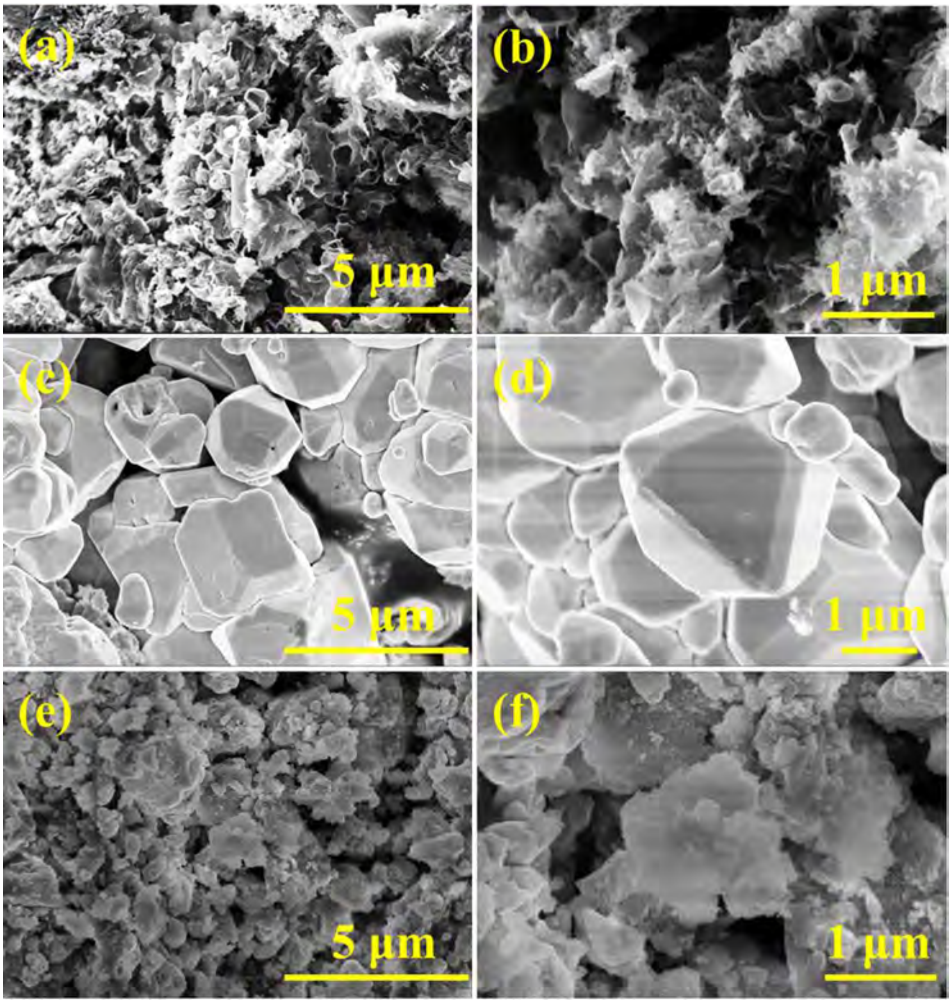

Fig. 2. SEM images of (a and b) PCNS, (c and d) $BiVO_4$ and (e and f) PCNS/BVO-400.

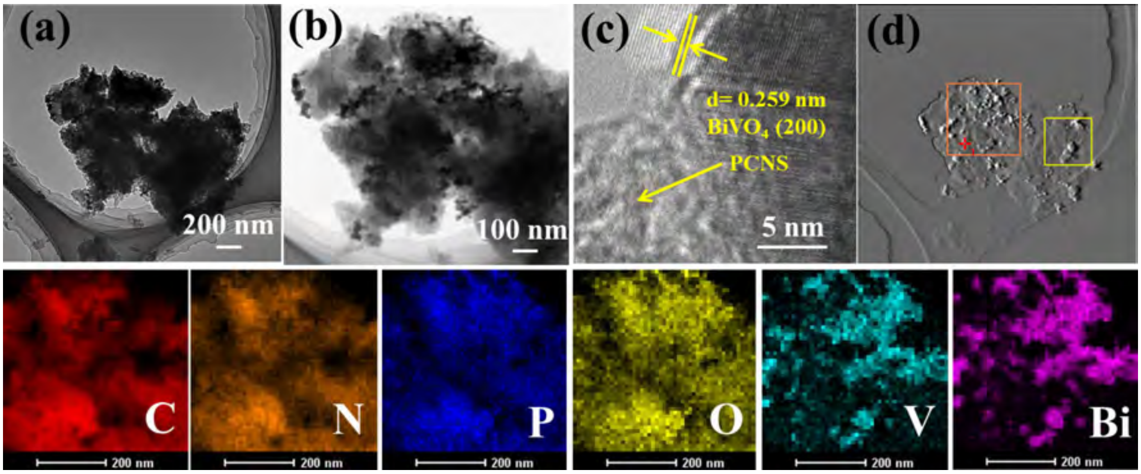

Fig. 3. TEM image (a and b), HR-TEM image (c) and STEM image (d) of PCNS/BVO-400, and the corresponding EDS mapping images of C, N, P, O, V and Bi elements in the red box area.

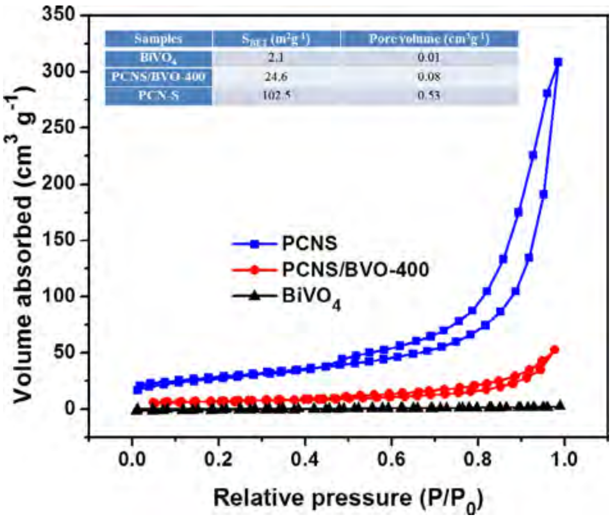

Samples	S_{BET} (m^2g^{-1})	Pore volume (cm^3g^{-1})
$BiVO_4$	2.1	0.01
PCNS/BVO-400	24.6	0.08
PCN-S	102.5	0.53

Fig. 4. N_2 adsorption-desorption isotherms of PCNS, $BiVO_4$ and PCNS/BVO-400.

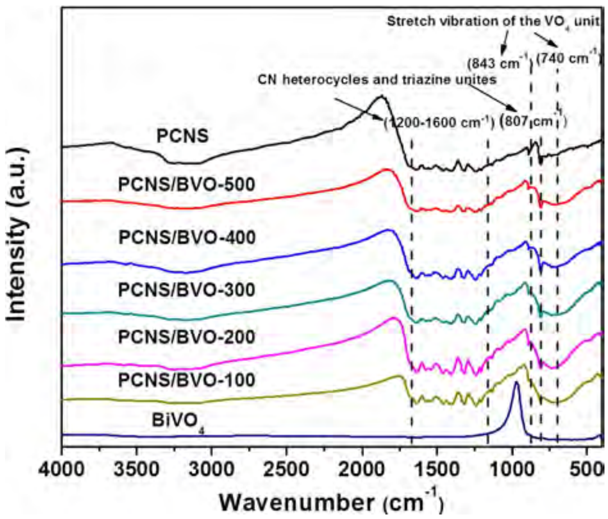

Fig. 5. FT-IR spectra of the prepared samples.

are 0.53, 0.01 and 0.08 cm^3/g, respectively. The results analysis mentioned above present that the prepared PCNS possess the highest specific surface areas. Besides, the prepared PCNS/BVO-400 nanocomposites also owns a relatively larger specific surface area than pure $BiVO_4$, providing more reaction sites than pure $BiVO_4$, which is in agreement with the adsorption performance of the prepared samples in the adsorption-equilibrium process.

3.3. Surface chemical composition and group analysis

To investigate the surface chemical composition and groups in the prepared samples, the relative FTIR spectra are provided and shown in Fig. 5. For the pure $BiVO_4$, one peak at 740 cm^{-1} can be identified as the v_3 asymmetric stretching vibration of the VO_4 unit v_3 (VO_4) and other peak at 843 cm^{-1} belongs to the v_1 symmetric stretching vibration of the VO_4 unit v_1 (VO_4), respectively [57,58]. As for pure PCNS, the typical FTIR spectra of g-C_3N_4 can be observed. In the region of 1200–1600 cm^{-1}, a series of peaks exist and belong to the typical stretching modes of CN heterocycles, and the peak locates at 807 cm^{-1} corresponding to the out of plane breathing vibration feature of triazine unites [52,59,60]. Furthermore, the FTIR spectra of all the prepared PCNS/$BiVO_4$ nanocomposites contain all characteristic peaks of PCNS and $BiVO_4$, indicating the co-existence of these two semiconductors [61].

The XPS measurement and analysis was employed to further investigate the surface chemical composition of the prepared PCNS/BVO-400, and the results are shown in Fig. 6. Fig. 6a presents the XPS survey spectrum of the prepared PCNS/BVO-400 sample, from which we can see the characteristic peaks of Bi, O, V, C and N elements, except the peaks of P element due to its relative low content in the composite. Fig. 6b-6g shows the high resolution spectra of Bi 4f, V 2p, O 1s, C 1s, N 1s and P 2p for the PCNS/BVO-400 composites, respectively. As shown in Fig. 6b, the peak locates at 164.31 eV belongs to the binding energy values of Bi $4f_{7/2}$ and another one at 159.04 eV refers to that of Bi $4f_{5/2}$. From the high-resolution XPS of V 2p (Fig. 6c), we can see that the two peaks at 516.4 eV and 524.01 eV can be attributed to the V $2p_{3/2}$ and V $2p_{1/2}$, respectively [57]. Fig. 6d shows the XPS spectra of O 1s, and it can be divided into five peaks. The peak at 529.8 eV is ascribed to the Bi-O bonds of $(Bi_2O_2)^{2+}$ in $BiVO_4$, and the peak at 530.97 eV is assigned to the hydroxyl groups (O—H) on the surface of the prepared sample [62]. Besides, the other two peaks at 532.67 eV and 533.49 eV are appeared, which refer to the formation of C═O and C—O during the oxidation process. Moreover, another peak locates at 531.89 eV also cannot be ignored, which

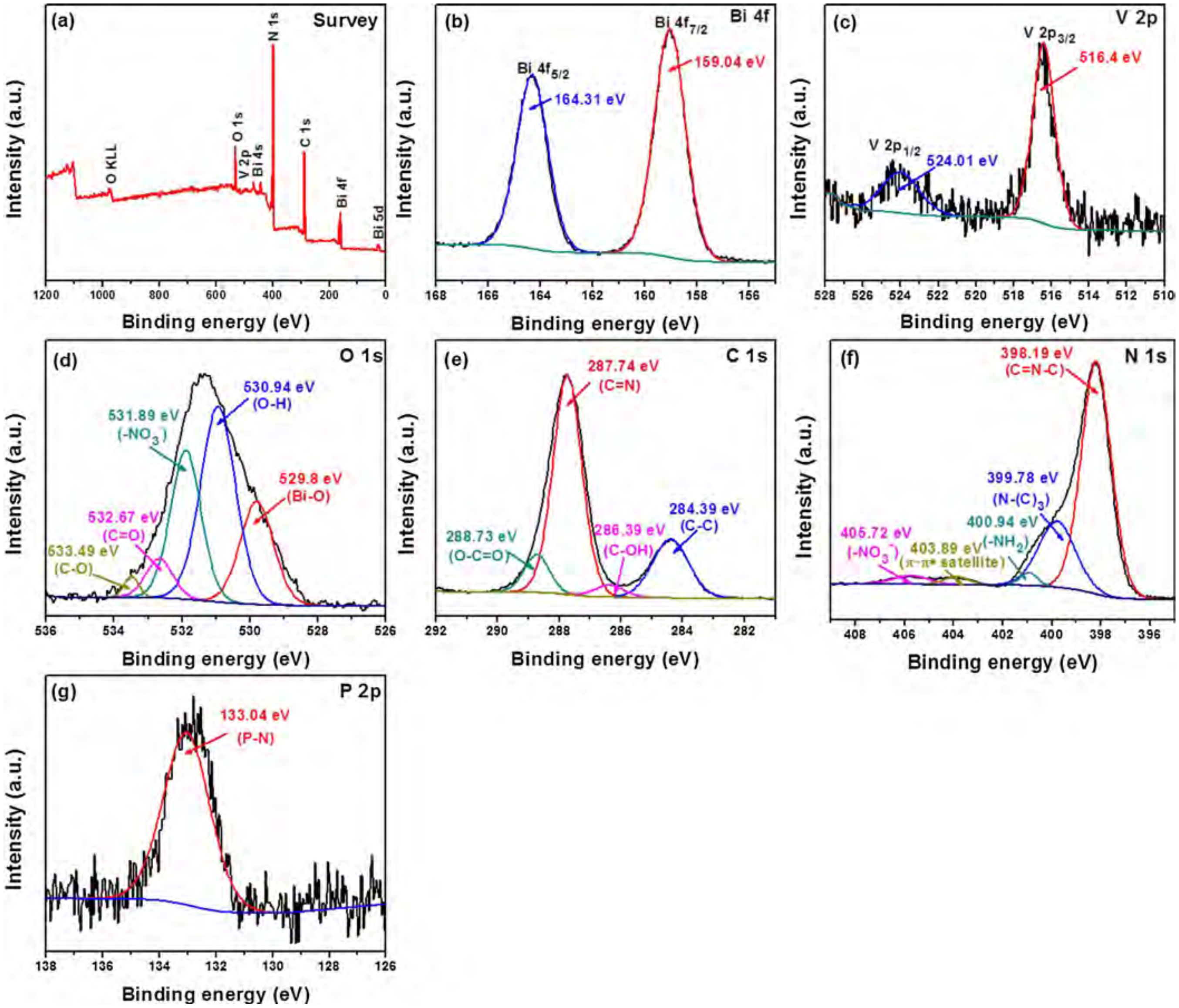

Fig. 6. The XPS spectra of PCNS/BVO-400.

represents the formation of $—NO_3^-$ during the acid treatment process. Fig. 6e shows the C 1s spectra, it can be seen that four independent peaks are obtained, one pair of peaks locates at 284.39 eV and 287.74 eV refer to the graphitic carbon (C—C) and sp^2-bounded carbon (C═N), respectively. Another pair of peaks at 286.39 eV and 288.73 eV represent the C—OH and carboxylate carbon (O—C═O), respectively. As for the XPS spectra of N 1s shown in Fig. 6f, it can be seen that the three peaks separated from the main peak are located at binding energies of 398.19 eV, 399.78 eV and 400.94 eV, representing the C═N—C, $N—(C)_3$ and $—NH_2$ groups, respectively. And meanwhile, at the binding energy of 403.89 eV and 405.72 eV appear other two minor peaks, which stand for the π-π∗ satellite and $—NO_3^-$, respectively [34]. As for P 2p, the main peaks of binding energy at 133.04 eV represents P-N band (Fig. 6g) [63]. Just as mentioned above, the existence of $—NO_3^-$ and the oxygen based groups in the prepared PCNS/BVO-400 strongly demonstrate the interaction between PCNS and $BiVO_4$, which ensure the high performance of the prepared nanocomposites in the photocatalytic degradation experiment. The XPS results further demonstrated that the PCNS/$BiVO_4$ composite was successfully obtained.

3.4. Optical properties

To investigate the optical property, the UV–vis DRS spectra of the prepared samples are provided and shown in Fig. 7a, from which we can see that the prepared PCNS shows great response ability in the visible light range and the response edge of the $BiVO_4$ is limited at 550 nm. For the prepared PCNS/BVO nanocomposites, the light response spectrum range is wider than pure $BiVO_4$ and has been broaden to 700 nm, which leads to more efficient light utilization ability.

To thoroughly understand the reason for the change of UV–vis DRS spectra of the prepared samples, the band gap (Eg) of PCNS and $BiVO_4$ has been analysis and calculated by the following formula [23,64]:

$$\alpha h\nu = A(h\nu - Eg)^{n/2} \quad (1)$$

where α, *h*, *ν*, Eg, and A are absorption coefficient, planck constant, light frequency, band gap energy, and a constant, respectively. The value of n is used as 1 for direct transition semiconductor and 4 for the indirect transition semiconductor. As reported in the previous literature, the n value of both $g\text{-}C_3N_4$ and $BiVO_4$ was 1 [50,64].

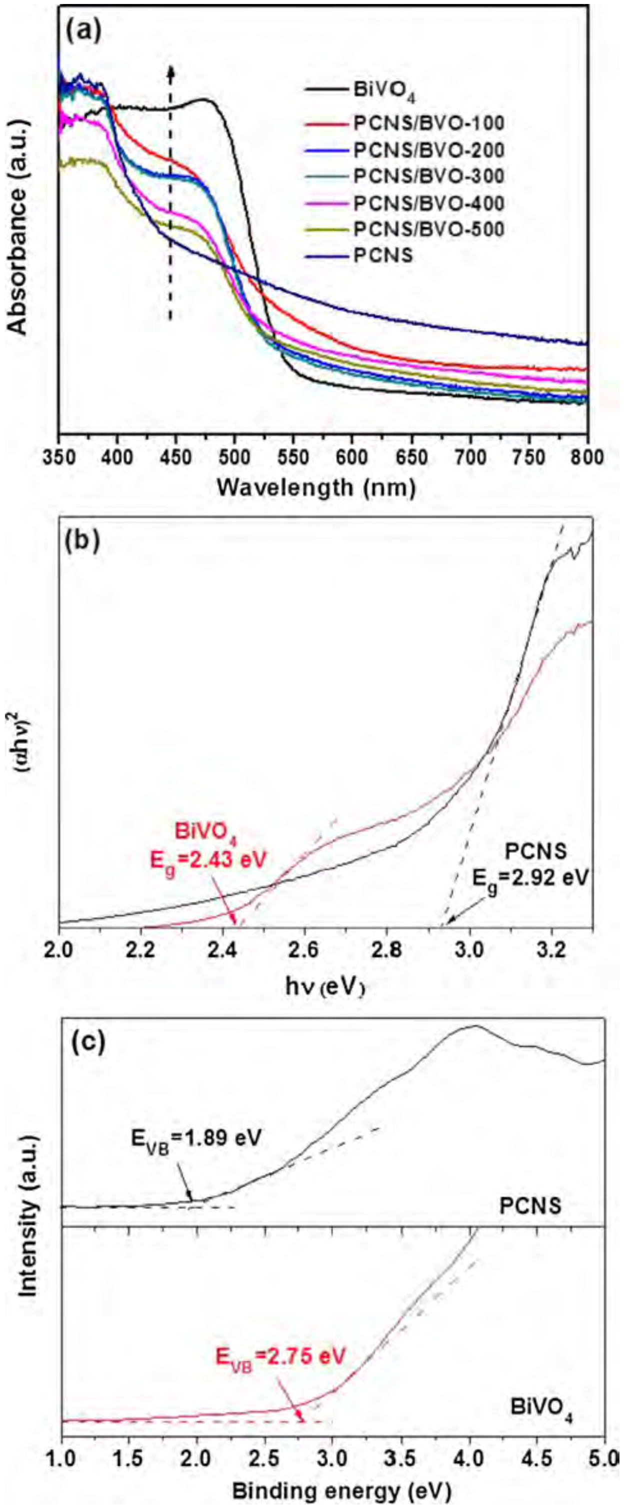

Fig. 7. (a) UV–Vis diffuse reflectance spectra of the prepared samples, (b) the band gap energy and (c) VB XPS spectra of PCNS and $BiVO_4$.

According to the information presents in Fig. 7b, the Eg of PCNS and $BiVO_4$ are estimated to be 2.92 eV and 2.43 eV, respectively. Moreover, to further understand the valence band of the prepared PCNS and $BiVO_4$, the XPS valence band data were collected and shown in Fig. 7c, from which we can see that the E_{VB} of PCNS and $BiVO_4$ are calculated as 1.89 eV and 2.75 eV, respectively. Besides, based on the results mentioned above, the E_{CB} of the prepared samples can be obtained according to follow equation [23]:

$$E_{CB} = E_{VB} - E_g \tag{2}$$

where Eg is the band gap of the sample, and E_{CB} and E_{VB} are the conduction band and valence band, respectively. Therefore, the E_{CB} of PCNS and $BiVO_4$ are −1.03 eV and +0.32 eV, respectively. These data are important for the description and explanation of the reaction process between PCNS and $BiVO_4$, and have been detailedly discussed in the reaction mechanism part.

3.5. Photoelectrochemical analysis and charge carrier life-time

Photoelectrochemical characteristics of the prepared samples are measured and analyzed to have a deep understanding of the photoresponse ability and the transfer properties, including photocurrent-time measurement (I-t), electrochemical impedance spectroscopy (EIS), and polarization curves. Fig. 8a shows the transient photocurrent responses produced by the pure PCNS, pure $BiVO_4$ and PCNS/BVO-400 samples. The photocurrent intensity of all the samples remained at a very low value in the light off condition, but increased quickly and kept at a relatively constant value when exposed to the visible light irradiation. The difference is that the PCNS/BVO-400 exhibits the highest photocurrent response ability than that of PCNS and $BiVO_4$. The higher photocurrent indicates the higher separation efficiency of the photogenerated charges. The results reflect from the photocurrent-time spectra indicate that the prepared PCNS/BVO-400 photocatalyst possesses excellent performance in photogenerated charge transfer and separation than the origin PCNS and $BiVO_4$. EIS measurement was employed to estimate the charge transfer process at the interfaces of photocatalysts and reaction solution. The smaller arc radius indicates the higher migration efficiency of charge. From the EIS Nyquist plot shown in Fig. 8b, we can see that the diameter of the arc radius belongs to the PCNS/BVO-400 composite electrode is smaller than those of the pure $BiVO_4$ and PCNS electrodes, which means that the rapid charge transfer and high photogenerated charges separation efficiency in the prepared PCNS/BVO-400 nanocomposites.

In addition, the polarization curve with the potential regions of −0.35 to −1.2 V vs Ag/AgCl for the samples was measured (Fig. 8c). As for PCNS/BVO-400, the much more cathodic current density indicates the boosted photocatalytic activity and photoresponse ability than that of PCNS and $BiVO_4$, which is in accordance with the photocatalytic performance on the PCNS/BVO-400 in the following photocatalytic degradation process. The results also indicate the synergistic effect between the PCNS and $BiVO_4$ plays the important role on the promoted photogenerated charge transfer rate and enhanced photocatalytic activity. To further demonstrate the recombination suppression, charge carrier lifetime in the reaction system was measured and analyzed [34]. As shown in Fig. 8d, the calculated lifetime (τ_1) of PCNS/BVO-400 is 1.65 ns, which is much longer than that of pure $BiVO_4$ (i.e., 0.82 ns). Moreover, the charge carrier lifetime of the prepared PCNS/BVO-400 is longer than that of pure PCNS (i.e., 1.46 ns), which indicates the synergistic effect between PCNS and $BiVO_4$ attributed to the fast transportation and the recombination inhibition of the photogenerated charges.

3.6. Photocatalytic performance of different photocatalysts

Fig. 9a shows the results of the as-prepared samples for the photocatalytic degradation of TC with the change of irradiation time. The result of the control experiment without photocatalysts means that the photolysis effect can be ignored during the photocatalytic degradation process. When the reaction system was operated with the addition of photocatalysts and exposed to the visible light irradiation condition, the concentration of TC was decreased

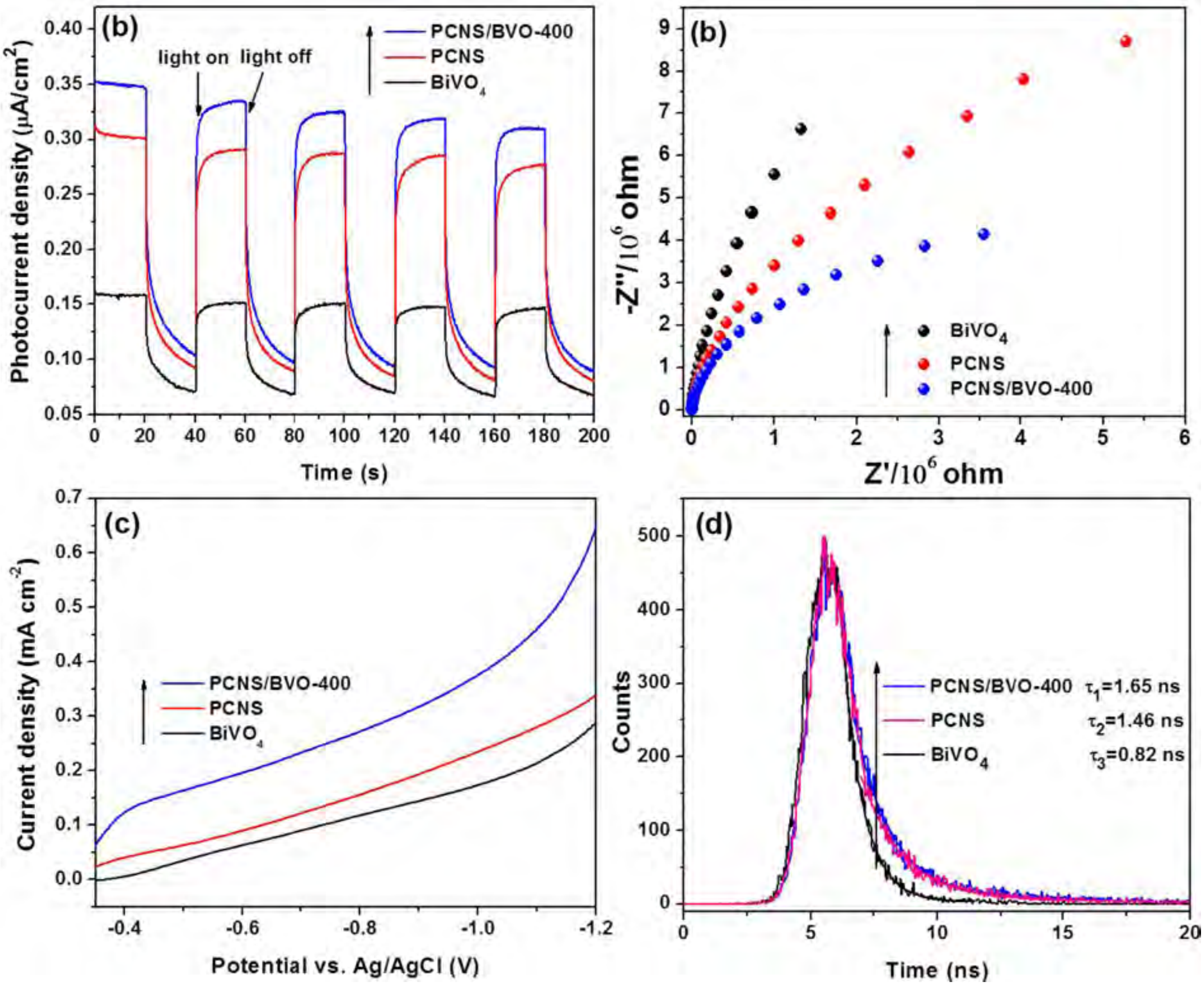

Fig. 8. (a) Photocurrent response (b) EIS Nyquist plots, (c) the cyclic voltammogram and (d) charge carrier lifetimes of PCNS, $BiVO_4$ and PCNS/BVO-400.

gradually. As for pure $BiVO_4$ samples, only 41.45% of TC was removed within 60 min under visible light irradiation. But for PCNS/BVO nanocomposites, the removal efficiency was improved and increased with the increasing content of PCNS contained in the composites. Besides, the highest removal efficiency of TC reached 96.65% for the prepared PCNS/BVO-400 sample within 60 min under visible light irradiation. However, further increasing the contents of PCNS in the prepared PCNS/BVO composites could not improve the photocatalytic performance anymore but cause the decreased photocatalytic activity. As for pure PCNS, only 71.78% removal efficiency of TC was obtained. For pristine CNS, the removal efficiency of TC was only 61.12% which was lower than that for PCNS. This result indicated that the phosphorus element doping can improve the photocatalytic activity of g-C_3N_4. Additionally, to make comparison, mechanical mixture of PCNS and $BiVO_4$ samples was also taken into consideration in this reaction system. From Fig. 9a, we can see that the photocatalytic performance of the Mechanical Mixed sample is poor than that of PCNS/BVO-400, which further demonstrates the reaction between the PCNS and $BiVO_4$ nanocomposite was important for the high photocatalytic activity of the prepared hybrid photocatalysts. It is well known that the adsorption ability of the photocatalysts play an important role for the eventual photocatalytic performance, so we deeply analyze the adsorption process of the prepared samples. As shown in Fig. 9b, the reaction system can reach adsorption-desorption equilibrium within 30 min under dark condition. The constructed PCNS/BVO nanocomposites present enhanced adsorption ability than pure $BiVO_4$, and the adsorption increase with the increase content of PCNS. Besides, the PCNS show the highest adsorption ability due to the highest specific surface area. The results of the adsorption process were in line with the BET analysis. The pseudo-first-order kinetic reaction kinetic values (k) were also calculated in Fig. 9c and d. it can be seen that the prepared PCNS/BVO-400 presented the highest reaction rate of 0.0492 min^{-1}, which was 4-fold of those for pure PCNS and 7-fold of $BiVO_4$. Besides, the reaction rate of the prepared PCNS is higher than CNS, which further demonstrated that P element doping boosts the photocatalytic activity of g-C_3N_4. The results mentioned above illustrated that the prepared PCNS/BVO-400 nanocomposites displays the optimum photocatalytic degradation performance, and the synergistic effect between PCNS and $BiVO_4$ attributed to the enhanced photocatalytic degradation efficiency.

3.7. The influence of photocatalyst dosage

Taken the practical applications into consideration, the cost of the photocatalyst occupied a large part in commercial consideration. So the effect of photocatalyst dosage on the photodegradation of TC based on PCNS/BVO-400 sample has been investigated. The dosage of the photocatalysts was studied in the range of 0.20–2.00 g/L. As shown in Fig. 10a, when the dosage of the prepared photocatalyst increases from 0.2 to 1.0 g/L, the relative photocatalytic removal efficiency towards TC increases from 58.95% to 96.95%. However, further increasing the photocatalyst dosage,

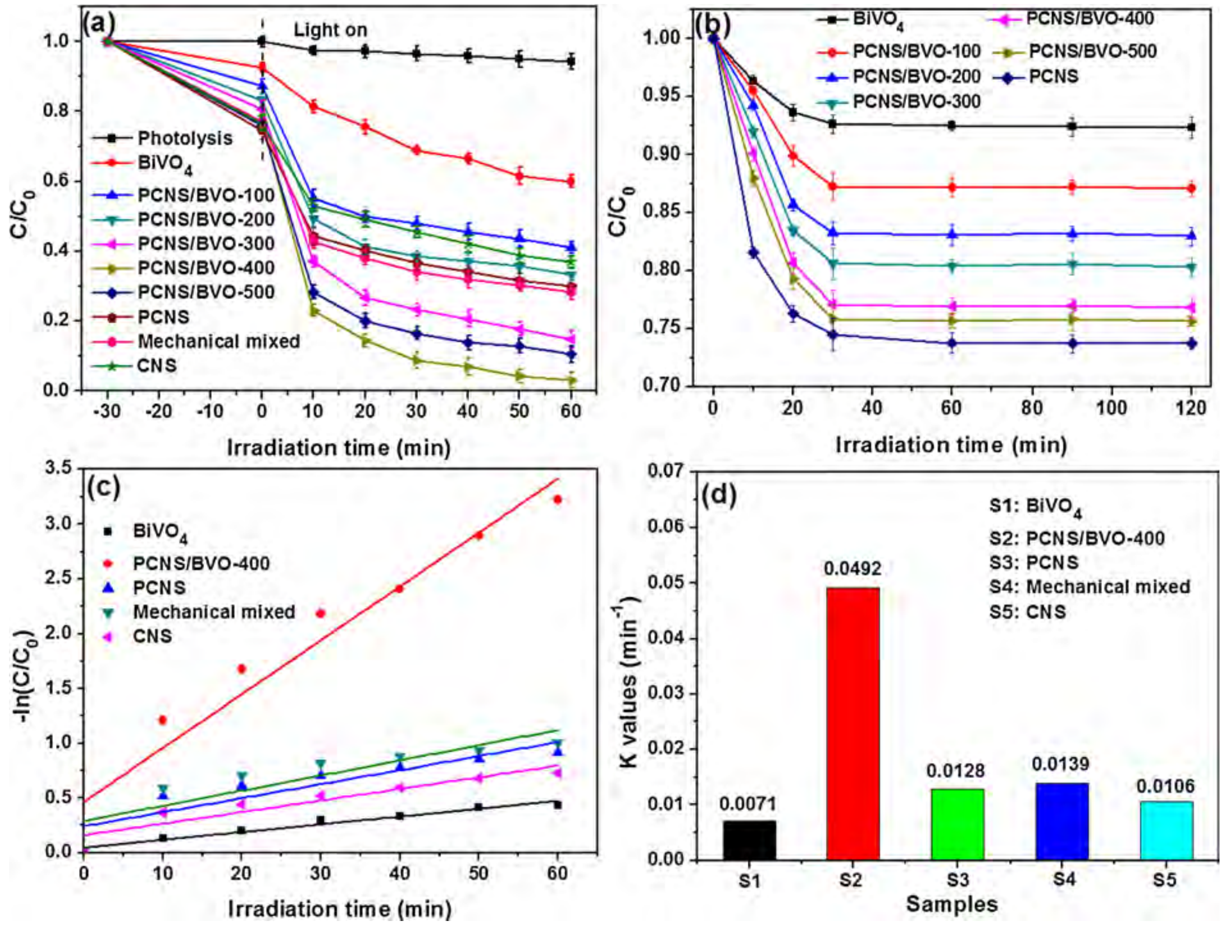

Fig. 9. (a) Photocatalytic degradation of TC with different photocatalysts under visible light irradiation; (b) Adsorption performance of the as-prepared photocatalysts toward TC in the dark. (c and d) the pseudo-first-order reaction kinetics of tetracycline based on different photocatalysts. (Experimental conditions: initial TC concentration = 10 mg/L, pH = 7.0, m = 100 mg, V = 100 mL, visible light: $\lambda > 420$ nm).

the photocatalytic efficiencies do not increase anymore, but experience a decrease process in the reaction system. The obtained results indicate that proper dosage of photocatalyst plays a vital role to acquire the optimum photocatalyst performance. This phenomenon can be explained in the following two aspects: on the one hand, higher photocatalyst dosage could provide more active site and species during the photocatalytic degradation process, which could improve the photocatalytic performance; on the other hand, when the dosage of photocatalyst was beyond the optimum value, redundant photocatalyst would increase the turbidity of the reaction solution and reduce the penetration of the irradiation light, which will inhibit the photocatalytic activity of the reaction system in a great extent. Therefore, without statement, the optimum photocatalyst dosage with 1.0 g/L was used in the following experiments

3.8. The influence of initial TC concentration

The initial concentration of the target pollutant also affects the performance of the photocatalysts, so the degradation of TC with different initial concentrations based on PCNS/BVO-400 reaction system has been investigated. As shown in Fig. 10b, the degradation efficiencies of TC decrease from 96.95% to 55.28% when the initial concentration of TC increase from 10 mg/L to 50 mg/L. The results means that higher initial contaminant concentration could bring about adverse influence on the photocatalytic process, due to the decreased transmission opportunity and path of the photon and reduced penetration rate of the irradiation light in the reaction solution. So less photon could migrate to the surface and active site of the photocatalyst. The similar results were also obtained by previous publications [38,65]. Moreover, the intermediates produced in the photocatalytic degradation process could occupy the limited reaction sites and compete with the TC molecules, and the competition was improved when the initial concentration of TC was increased, causing the relative low removal efficiency. Therefore, to make full use of the photocatalytic activity of the photocatalyst and decrease the effect of the TC concentration for the analysis of this study, the 10 mg/L of the initial TC concentration was picked out in the whole experiments.

3.9. The influence of different pH value

The pH value of the solution plays an important role in the photocatalytic reaction and affects the surface charge properties and the adsorption ability of PCNS/BVO-400. So the influence of different pH value in the reaction system has been conducted, and the result is shown in Fig. 10c. Point of zero charge (PZC) is a reliable value for the evaluation of the surface charge of the photocatalyst during the photocatalytic process. The PZC of the prepared PCNS/BVO-400 is pH 5.78 (Fig. S1) [66]. So when the solution pH is below 5.78, especially at pH 3, both of the TC molecular and the surface of the PCNS/BVO-400 are positively charged, and the strong repulsion would inhibit the adsorption of TC on the surface of the photocatalysts, which will decrease the degradation efficiency. When the

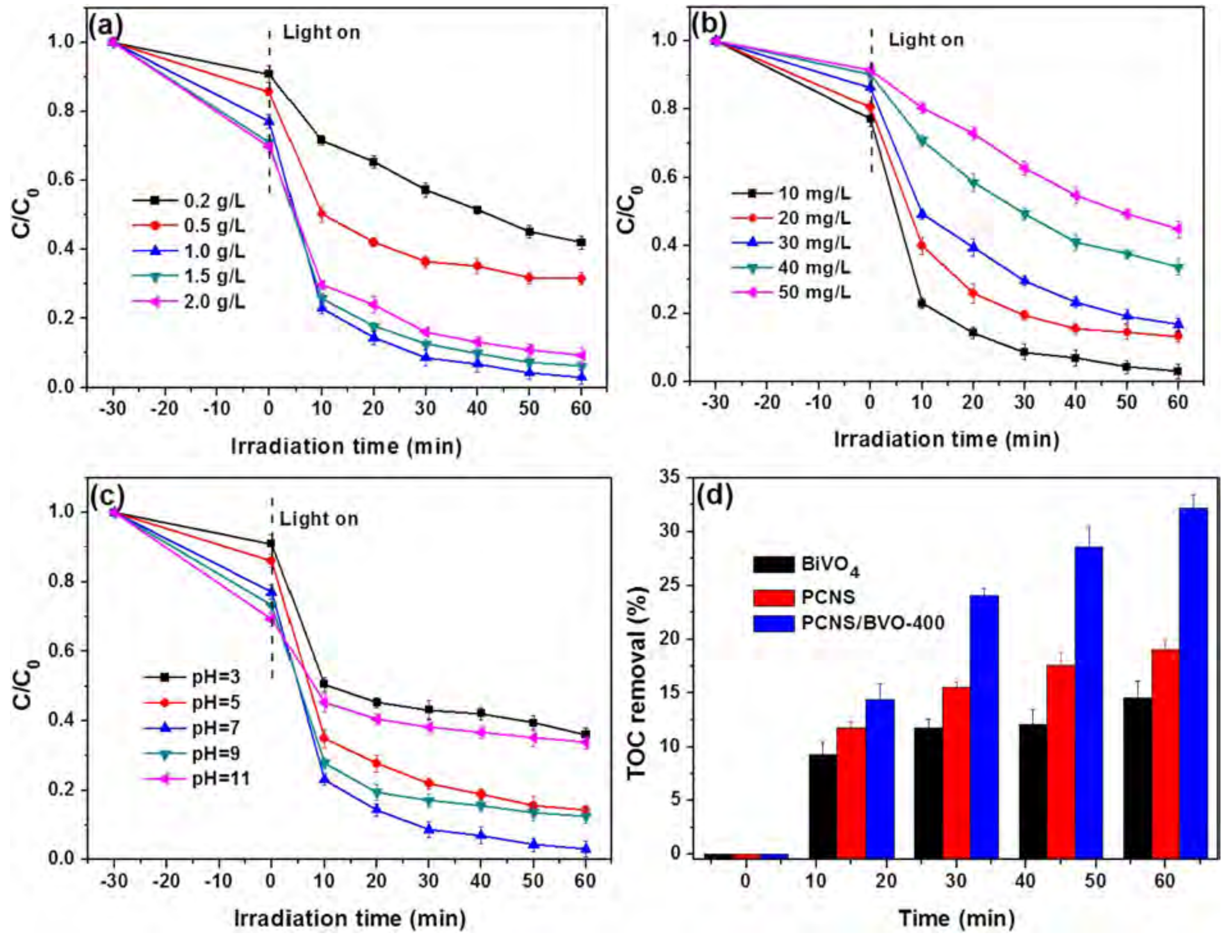

Fig. 10. The influence of (a) photocatalysts dosage; (b) initial TC concentration; (c) initial pH value for the photocatalytic activity of PCNS/BVO-400 nanocomposite and (d) total organic carbon (TOC) removal efficiency of the prepared PCNS, $BiVO_4$ and PCNS/BVO-400 nanocomposites under visible light irradiation.

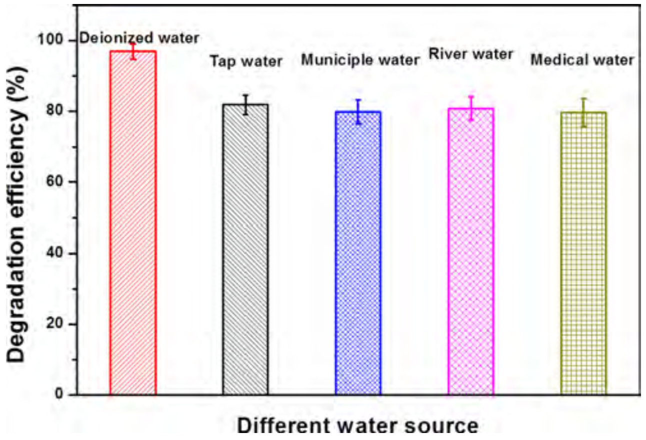

Fig. 11. The influence of different water sources on the degradation of TC over PCNS/BVO-400 nanocomposite under visible light irradiation.

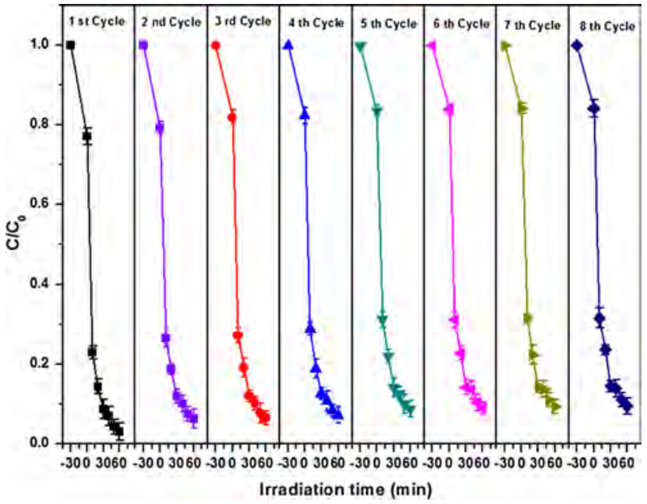

Fig. 12. Recycle experiments of PCNS/BVO-400 nanocomposites for the photocatalytic degradation of TC. (Experimental conditions: initial TC concentration = 10 mg/L, pH = 7, M = 100 mg, V = 100 mL, visible light: λ > 420 nm).

solution pH is above 5.78, the opposite charge will lead to the improved adsorption ability between the TC and photocatalyst due to the developed electrostatic attraction. However, the strong electrostatic attraction would lead to the strong adsorption of the TC molecules on the surface of the catalysts, which will cause the decrease of the reaction sites and the absorption of the light on the catalysts. Besides, the strong adsorption results in a multilayer of TC molecules covered the catalyst surface, which means that the molecules cannot contact with the catalyst directly [67]. Moreover, the negatively charged photocatalysts in high pH value suppress the adsorption of hydroxide ions, leading to the decreased formation of hydroxyl radicals. That is the reason why at pH 11, the degradation efficiency was greatly decreased. Owing to the large

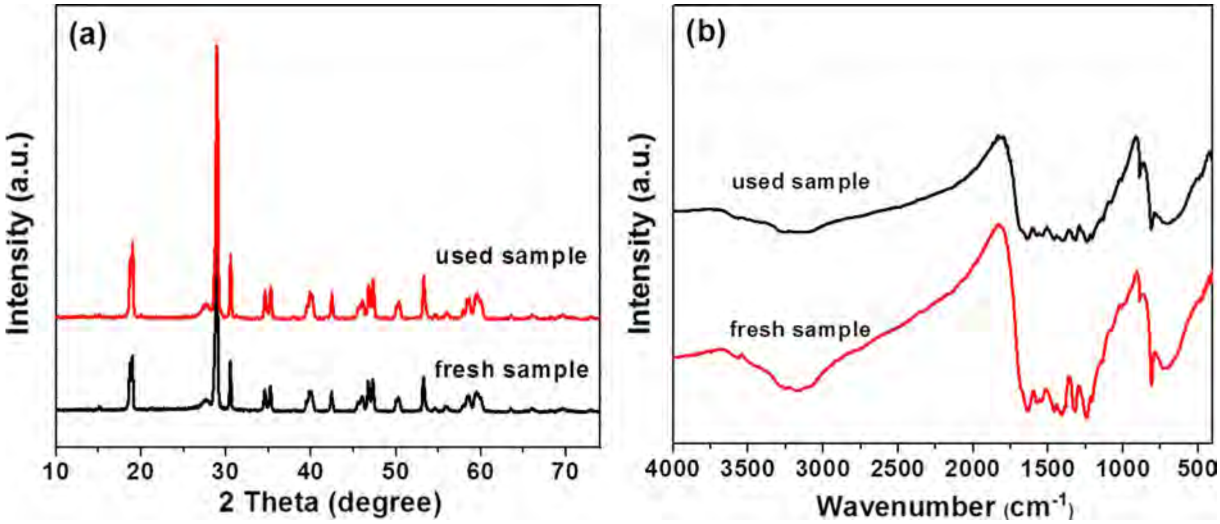

Fig. 13. (a) XRD patterns and (b) FTIR spectra of the fresh and used PCNS/BVO-400 nanocomposite.

Table 1
The information of the intermediates.

Compounds	Formula	*m*/*z*	Proposed structure
NO1	C22H24N2O8	445	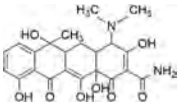
NO2	C22H24N2O9	461	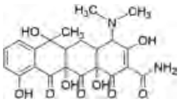
NO3	C22H24N2O9	461	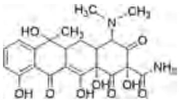
NO4	C22H24N2O9	461	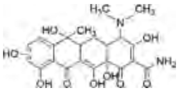
NO5	C22H24N2O10	477	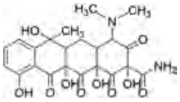
NO6	C22H24N2O10	477	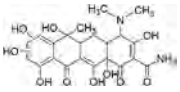
NO7	C22H22N2O11	490	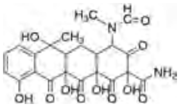
NO8	C22H26N2O11	495	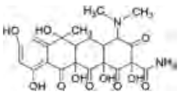
NO9	C22H24N2O10	459	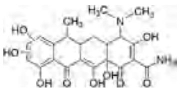
NO10	C22H22N2O7	427	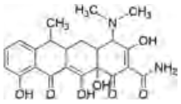
NO11	C21H22N2O8	431	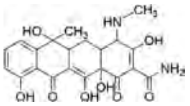
NO12	C20H20N2O8	417	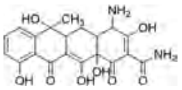
NO13	C21H22N1O8	417	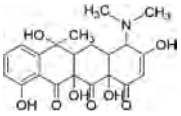

photocatalytic performance of the prepared photocatalyst at pH 7.0, the following experiments were conducted at this pH value.

3.10. Mineralization ability tests

To further evaluate the mineralization ability of this reaction system, total organic carbon (TOC) removal efficiencies have been conducted. As disclosed in Fig. 10d, after 60 min of visible light irradiation, mineralization rates of 14.58%, 19.09% and 32.21% are obtained for the pure $BiVO_4$, pure PCNS and PCNS/BVO-400, respectively, indicating that the prepared PCNS/BVO-400 not only presents enhanced TC degradation efficiency, but also performs improved mineralization ability.

3.11. The influence of different water sources

Taking the realistic application into consideration, the initial status of the reaction matrix will greatly affects the photocatalytic performance, so different water sources were used as the reaction solutions for the removal of TC by PCNS/BVO-400 nanocomposites. Municipal water and medical water which have been primarily treated as the solvents and spiked with TC to investigate the photocatalytic activity of the prepared samples, and analyzed whether the different water resources would affect the photocatalytic performance. The river water was collected from Xiangjiang River. As shown in Fig. 11, the degradation efficiencies of TC in deionized water, tap water, river water, municipal wastewater and medical wastewater are 96.95%, 81.88%, 80.81%, 78.87% and 79.62%, respectively. It should be noted that although the removal efficiencies in the real samples are slightly lower compared with that in deionized water due to the existence of various competitive substances, they are still very high. Hence, the results indicated that the prepared PCNS/BVO-400 nanocomposites possessed the potential for realistic wastewater treatment and recovery.

3.12. Photocatalyst recyclability

As for realistic applications, the recyclability of the photocatalysts is a very important factor. The reaction process of the prepared PCNS/BVO-400 towards TC degradation was repeated for five times. After the reaction, the photocatalyst was collected, washed and dried for next cycle test. As the results displayed in Fig. 12, even after eight recycles, the degradation rate of TC by PCNS/BVO-400 photocatalyst still reaches 90.51%, which indicated the high stability and good performance of the photocatalyst. Besides, to further study the structure and chemical stability of the photocatalyst, the XRD and FTIR analysis of the samples before and after photocatalytic reaction are provided to make comparison. As shown in Fig. 13a and b, the XRD pattern and FTIR spectra of the used PCNS/BVO-400 nanocomposites nearly stay the same as that of fresh samples. The results demonstrated the excellent stability of the prepared PCNS and $BiVO_4$ hybrid photocatalysts.

3.13. Identification of intermediates and the proposed degradation pathway

To deeply understand the degradation process of TC, LC-MS/MS was employed to identify the degradation intermediates and help to propose the reaction mechanism. Several typical intermediates were tentatively identified in the solution (see Table 1). For pure TC solution, the solo peak with m/z of 445 can be directly observed (Fig. S2a), and no other intermediate was detected after 30 min adsorption (Fig. S2b). In the photodegradation process, the intensity peak of TC was decreased and some intermediates with the m/z of 495, 490, 477, 461, 459, 431, 427, and 417 were appeared after 30 min light irradiation (Fig. S2c). These main intermediates were generated in N-demethylation process and hydroxylation process, and the degradation pathway was proposed and presented in Fig. 14. The hydroxylation process was also reported by other groups that $^{\cdot}OH$ radicals can attack various positions of TC to produce different hydroxylated products of TC [6,68]. Besides, some intermediates with relative smaller m/z can be observed, which can be attributed to the N-demethylation process due to the h^+ attack process of TC molecular. After 60 min irradiation, the TC molecular ion with m/z of 445 almost disappeared, which was consistent with the results in the degradation process (Fig. S2d). According to the aforementioned results, the photocatalytic decomposition of TC was mainly via two processes: N-demethylation process and hydroxylation process. On the one hand, owing to the low bond energy of N-C, the N-demethylation process would happen, which resulted in the generation of the intermediates with m/z of 431 and 417 [69]. On the other hand, the produced $^{\cdot}OH$ active species can directly reacted with TC molecular in the hydroxylation reaction [70]. Then two anions with m/z of 461 and 477 were observed. But for the products with the m/z of 461, three different products were obtained due to $^{\cdot}OH$ attack in different reaction sites of TC molecular. When the product

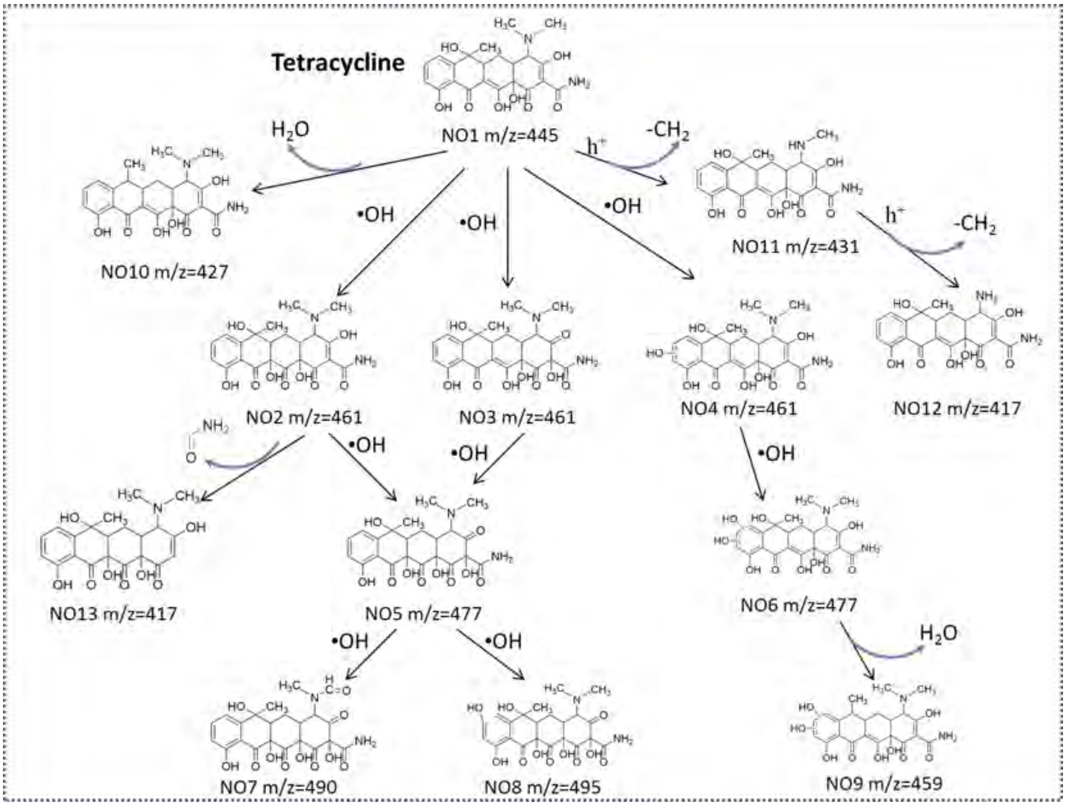

Fig. 14. The proposed photocatalytic degradation pathway of TC.

with *m*/*z* of 461 was further degraded by ·OH, and the compounds with *m*/*z* of 477, 490 and 495 were produced. Moreover, the dehydration process also happened due to the attack process by ·OH, which resulted in the production of product with *m*/*z* of 427, or the further degradation product of 477 with the *m*/*z* of 459. These results affirmed that the generated intermediates were degraded progressively in the photocatalytic degradation process.

3.14. Possible photocatalytic reaction mechanism

It is well know that the radical species play the major role in the photocatalytic degradation process. To explore the predominant active species for TC degradation in the reaction system, three typical scavengers, isopropanol (IPA), ethylenediamintetraacetic acid disodium (EDTA-Na_2) and 1,4-benzoquinone (BQ) were used for the estimation of hydroxyl radical (·OH), hole (h^+) and superoxide radical ($\cdot O_2^-$), respectively [23,38,54]. The concentration of the above three scavengers added in the reaction system were 1 mM. As displayed in Fig. 15a, when the EDTA-Na_2 was added into the reaction system as the scavenger for h^+ species, the photocatalytic process has been inhibited greatly, and the removal efficiency of TC decrease from 96.95% to 46.24%, indicating the h^+ affect the decomposition of TC greatly. Similarly, the removal rate of TC was also greatly suppressed with the addition of BQ, indicating the $\cdot O_2^-$ radical species also plays crucial role towards TC degradation. In order to affirm the function of $\cdot O_2^-$, a parallel experiment was conducted under purging the N_2 without the addition of any scavenges. The result shows that the TC degradation efficiency also decreased greatly under N_2 ambient condition, implying that the dissolved oxygen can react with the photogenerated electrons for the formation of O_2^- radical species. Moreover, when the IPA was added as the ·OH species, the removal efficiency of TC was decreased in some extent, implying that the ·OH was also produced and participated in the photodegradation process. According to the results mentioned above, we can preliminarily ascertain that h^+ and $\cdot O_2^-$ are the dominant species in this reaction system, and meanwhile, ·OH also plays a certain role in TC degradation process.

To further affirm the existence of the radical species in the reaction system, the ESR spin-trap with the addition of DMPO agent was conducted on PCNS/BVO-400 nanocomposites under visible light irradiation. The detection of the reaction radical species is conducted with two parts: one part is operated under dark condition; and the other is carried out under visible light irradiation for 5 min, 10 min and 15 min. The results of DMPO-$\cdot O_2^-$ are shown in Fig. 15b. It can be seen that under dark conditions, no signal can be found, while under visible light irradiation, strong DMPO-$\cdot O_2^-$ adducts appear, suggesting that large amount of $\cdot O_2^-$ were produced and participate the TC degradation process. Similarly, the characteristic signals of ·OH are also can be observed in the measure system under visible light irradiation, and the signals can be ignored under dark condition. This phenomenon also indicates that ·OH was also generated in this reaction system and took part in the photocatalytic reaction process (Fig. 15c). To sum up, h^+ and $\cdot O_2^-$ species played the major role for TC degradation in the photocatalytic reaction system, and meanwhile, ·OH species also participated in the photocatalytic reaction process, and contributed to the enhanced performance in some extent.

It is generally accepted that the overall performance of the photocatalysts was determined by many factors, such as the photoresponse ability, photogenerated electron-holes transportation rate and specific surface areas. In this study, the enhanced photocatalytic degradation ability based on PCNS and $BiVO_4$ hybrid nanocomposites toward TC removal have been investigated, and the characteristics of optical ability, light response and transfer of photogenerated electron and holes have also been investigated in detail. Therefore, based on the above experimental results and analysis, we proposed a Z-scheme mechanism for the TC degradation over PCNS/BVO hybrid nanocomposites, and this mechanism process is shown in Scheme 2. It can be seen that under visible light irradiation, both of PCNS and $BiVO_4$ would generate electron and holes. According to the traditional heterojunction and band to band transfer process, the photogenerated electrons in the CB of PCNS would transfer to the CB of $BiVO_4$, and the VB holes of $BiVO_4$ would migrate to VB of PCNS, and then this transfer process

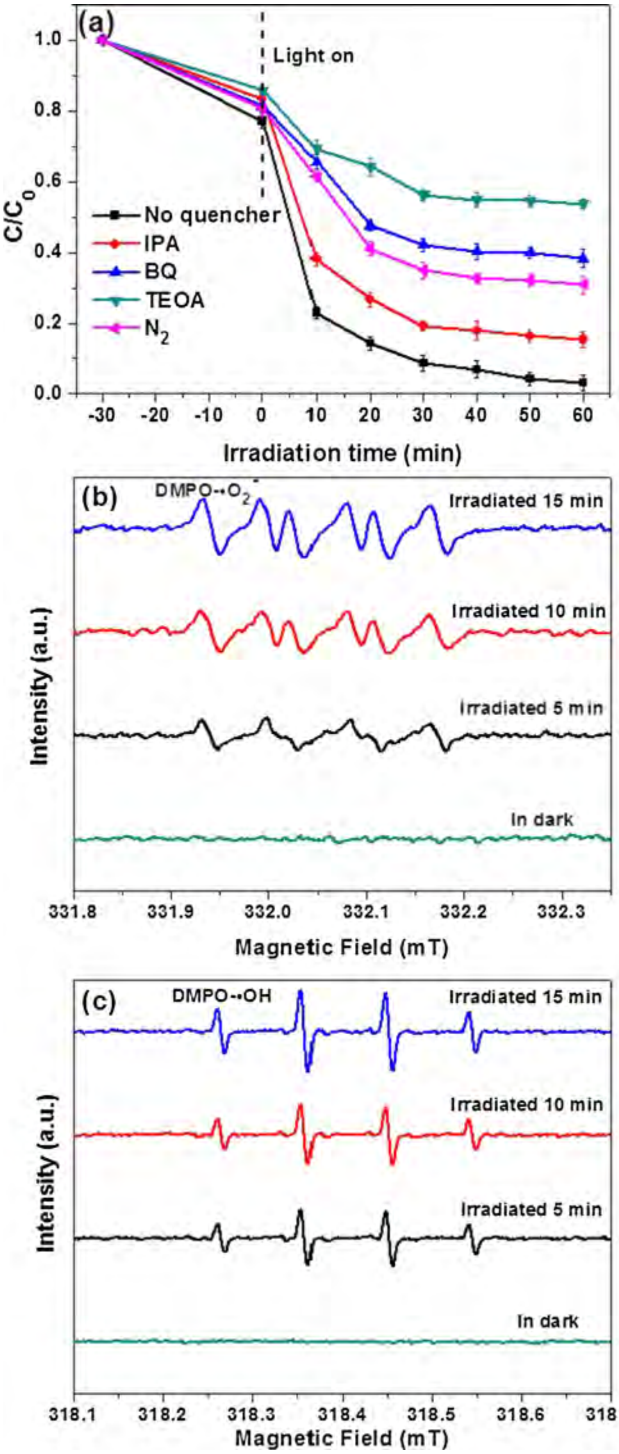

Fig. 15. (a) Trapping experimental of active species for the photocatalytic degradation of TC over PCNS/BVO-400 nanocomposite under visible light irradiation; ESR spectra of radical adducts trapped by DMPO ($\cdot O_2^-$ and ·OH) in PCNS/BVO-400 nanocomposite in the dark and under visible light irradiation: (b) in methanol dispersion for DMPO-$\cdot O_2$- and (c) in aqueous dispersion for DMPO-·OH.

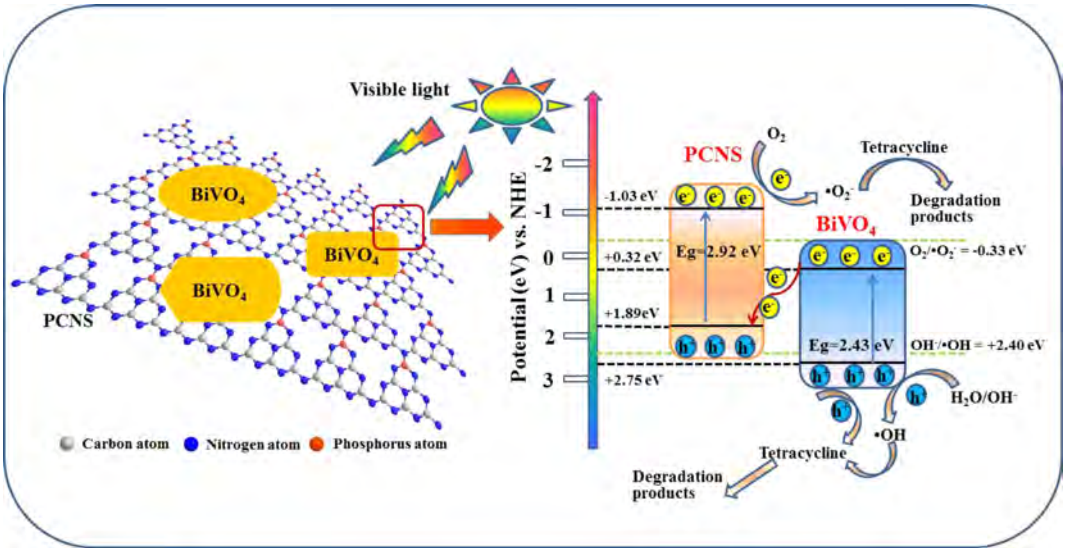

Scheme 2. Schematic illustration of the proposed reaction mechanism in the phosphorous-doped ultrathin g-C_3N_4 nanosheets/$BiVO_4$ nanocomposites based reaction system towards TC degradation under visible light irradiation.

contributes to the separation of the photogenerated electron and hole. Besides, based on the analysis mentioned above, the band energy of PCNS was 2.92 eV, and the CB and VB of PCNS was -1.03 eV and 1.89 eV, respectively. The band energy of $BiVO_4$ was 2.43 eV, and the corresponding CB and VB was 0.32 eV and 2.75 eV, respectively. The CB of $BiVO_4$ was not more negative than that of $O_2/{}^{\cdot}O_2^-$ (−0.33 eV), and the VB of PCNS was not more positive than that of $OH^-/{}^{\cdot}OH$ (2.4 eV) [23], which means that the ${}^{\cdot}O_2^-$ and ${}^{\cdot}OH$ species cannot be generated based on the traditional heterojunction transfer process. However, the ${}^{\cdot}O_2^-$ and ${}^{\cdot}OH$ species have been demonstrated to be generated and participated in this photocatalytic reaction system, so the Z-scheme mechanism was more appropriate to describe the reaction process. That is to say, the photogenerated electrons generated on the CB of $BiVO_4$ prefer to transfer to the VB of PCNS and recombine with the remained holes. Then the electrons in the CB of PCNS react with dissolved O_2 to generated ${}^{\cdot}O_2^-$ for TC degradation. The holes in the VB of $BiVO_4$ would participate in the reaction process via two pathways: on one hand, the holes can react with TC directly; and on the other hand, the holes can also react with H_2O to produce ${}^{\cdot}OH$, and then degrade TC to its degradation products. And meanwhile, due to the absence of the transfer process, the remained electrons and holes in CB of PCNS and VB of $BiVO_4$ possessed strong redox ability, which is an important factor attributed to the enhanced photocatalytic performance based on the prepared PCNS and $BiVO_4$ hybrid nanocomposites.

4. Conclusion

All in all, PCNS/BVO Z-scheme photocatalyst was synthesized by a simple acid treated and hydrothermal procedure. The synthesized PCNS/BVO-400 showed the optimum photocatalytic activity for 96.95% removal efficiency of TC within 60 min under visible light, which was higher than that of pure PCNS and $BiVO_4$. The boosted photocatalytic activity and removal efficiency can be attributed to the synergistic effects of PCNS and $BiVO_4$. The enhanced light response ability in the whole spectrum and the larger specific surface area of the PCNS in the reaction process can provide large amount of reaction site and lead to high photocatalytic performance. The intimate connect and the match of the band gap can promote the transfer and separation of the photogenerated electron and holes. Meanwhile, to make in-depth understand the decomposition process of the TC molecules, HPLC-MS/MS technology was also employed into the study, and we found that the N-demethylation process and hydroxylation process were the main degradation processes for TC in this reaction system. It should be noted that high degradation efficiencies towards TC removal were also achieved by PCNS/BVO-400 in real water sources, indicating the great potential for realistic employment in further wastewater treatment.

Acknowledgments

The study was financially supported by Projects 51579096, 51521006, 51222805, 51508175 and 51409024 supported by National Natural Science Foundation of China, the National Program for Support of Top–Notch Young Professionals of China (2012), the Program for New Century Excellent Talents in University from the Ministry of Education of China (NCET-11-0129), the Hunan Province Innovation Foundation for Postgraduate (CX2015B095).

Appendix A. Supplementary material

Supplementary data associated with this article can be found, in the online version, at http://dx.doi.org/10.1016/j.jcis.2017.09.016.

References

[1] S. Kim, P. Eichhorn, J.N. Jensen, A.S. Weber, D.S. Aga, Environ. Sci. Technol. 39 (2005) 5816.
[2] I. Chopra, M. Roberts, Microbiol. Mol. Biol. Rev. 65 (2001) 232.
[3] S. Leong, D. Li, K. Hapgood, X. Zhang, H. Wang, Appl. Catal. B – Environ. 198 (2016) 224.
[4] L. Tang, G.M. Zeng, G.L. Shen, Y.P. Li, Y. Zhang, D.L. Huang, Environ. Sci. Technol. 42 (2008) 1207.
[5] C. Zhang, C. Lai, G. Zeng, D. Huang, C. Yang, Y. Wang, Y. Zhou, M. Cheng, Water Res. 95 (2016) 103.
[6] J. Jeong, W. Song, W.J. Cooper, J. Jung, J. Greaves, Chemosphere 78 (2010) 533.
[7] Z. Li, L. Zhu, W. Wu, S. Wang, L. Qiang, Appl. Catal. B-Environ. 192 (2016) 277.
[8] H. Wang, X. Yuan, Y. Wu, G. Zeng, H. Dong, X. Chen, L. Leng, Z. Wu, L. Peng, Appl. Catal. B – Environ. 186 (2016) 19.
[9] E.A. Auerbach, E.E. Seyfried, K.D. McMahon, Water Res. 41 (2007) 1143.
[10] L. Rizzo, C. Manaia, C. Merlin, T. Schwartz, C. Dagot, M.C. Ploy, I. Michael, D. Fatta-Kassinos, Sci. Total. Environ. 447 (2013) 345.
[11] Y. Liu, X. He, X. Duan, Y. Fu, D. Fatta-Kassinos, D.D. Dionysiou, Water Res. 95 (2016) 195.

[12] A.K. Sarmah, M.T. Meyer, A.B. Boxall, Chemosphere 65 (2006) 725.
[13] X. Zhu, Y. Liu, F. Qian, C. Zhou, S. Zhang, J. Chen, Biores. Technol. 154 (2014) 209.
[14] B. Kakavandi, A. Takdastan, N. Jaafarzadeh, M. Azizi, A. Mirzaei, A. Azari, J. Photoch. Photobi. A 314 (2016) 178.
[15] C.V. Gómez-Pacheco, M. Sánchez-Polo, J. Rivera-Utrilla, J. López-Peñalver, Chem. Eng. J. 178 (2011) 115.
[16] R. Hao, X. Xiao, X. Zuo, J. Nan, W. Zhang, J. Hazard. Mater. 209–210 (2012) 137.
[17] W. Wang, J. Fang, S. Shao, M. Lai, C. Lu, Appl. Catal. B: Environ. 217 (2017) 57.
[18] X. Xiao, R. Hu, C. Liu, C. Xing, X. Zuo, J. Nan, L. Wang, Chem. Eng. J. 225 (2013) 790.
[19] C.Y. Wang, H. Zhang, F. Li, L.Y. Zhu, Environ. Sci. Technol. 44 (2010) 6843.
[20] C. Chang, L. Zhu, S. Wang, X. Chu, L. Yue, A.C.S. Appl, Mater. Interfaces 6 (2014) 5083.
[21] L. Tang, Y.C. Deng, G.M. Zeng, W. Hu, J.J. Wang, Y.Y. Zhou, J.J. Wang, J. Tang, W. Fang, J. Alloys Compd. 662 (2016) 516.
[22] Y.C. Deng, L. Tang, G.M. Zeng, H.R. Dong, M. Yan, J.J. Wang, W. Hu, J.J. Wang, Y. Y. Zhou, J. Tang, Appl. Surf. Sci. 387 (2016) 882.
[23] Y.C. Deng, L. Tang, G.M. Zeng, J.J. Wang, Y.Y. Zhou, J.J. Wang, J. Tang, Y.N. Liu, B. Peng, F. Chen, J. Mol. Catal. A-Chem. 421 (2016) 209.
[24] L. Tang, J.J. Wang, G.M. Zeng, Y.N. Liu, Y.C. Deng, Y.Y. Zhou, J. Tang, J.J. Wang, Z. Guo, J. Hazard. Mater. 306 (2015) 295.
[25] Y. Hou, F. Zuo, A. Dagg, P. Feng, Nano Lett. 12 (2012) 6464.
[26] S. Zhang, H. Gao, J. Li, Y. Huang, A. Alsaedi, T. Hayat, X. Xu, X. Wang, J. Hazard. Mater. 321 (2017) 92.
[27] S. Zhang, H. Gao, X. Liu, Y. Huang, X. Xu, N.S. Alharbi, T. Hayat, J. Li, A.C.S. Appl, Mater. Interf. 8 (2016) 35138.
[28] S. Zhang, H. Yang, H. Gao, R. Cao, J. Huang, X. Xu, A.C.S. Appl, Mater. Interf. 9 (2017) 23635.
[29] S. Zhang, Q. Fan, H. Gao, Y. Huang, X. Liu, J. Li, X. Xu, X. Wang, J. Mater. Chem. A 4 (2016) 1414.
[30] N.C. Castillo, A. Heel, T. Graule, C. Pulgarin, Appl. Catal.B – Environ. 95 (2010) 335.
[31] A. Kudo, K. Omori, H. Kato, J. Am. Chem. Soc. 121 (1999) 11459.
[32] M. Ge, L. Liu, W. Chen, Z. Zhou, CrystEngComm 14 (2012) 1038.
[33] Y. Deng, L. Tang, G. Zeng, C. Feng, H. Dong, J. Wang, H. Feng, Y. Liu, Y. Zhou, Y. Pang, Environ. Sci. Nano 4 (2017) 1494.
[34] H.J. Kong, D.H. Won, J. Kim, S.I. Woo, Chem. Mater. 28 (2016) 1318.
[35] M. Ge, Y. Li, L. Liu, Z. Zhou, W. Chen, J. Phys. Chem. C 115 (2011) 5220.
[36] Y. Wang, Q. Wang, X. Zhan, F. Wang, M. Safdar, J. He, Nanoscale 5 (2013) 8326.
[37] P. Zhou, J. Yu, M. Jaroniec, Adv. Mater. 26 (2014) 4920.
[38] F. Chen, Q. Yang, X. Li, G. Zeng, D. Wang, C. Niu, J. Zhao, H. An, T. Xie, Y. Deng, Appl. Catal.B – Environ. 200 (2017) 330.
[39] K. Maeda, D. Lu, K. Domen, ACS Catal. 3 (2013) 1026.
[40] Y. Sasaki, A. Iwase, H. Kato, A. Kudo, J. Catal. 259 (2008) 133.
[41] Y. Sasaki, H. Kato, A. Kudo, J. Am. Chem. Soc. 135 (2013) 5441.
[42] L. Ye, J. Liu, C. Gong, L. Tian, T. Peng, L. Zan, ACS Catal. 2 (2012) 1677.
[43] J. Zhang, M. Zhang, C. Yang, X. Wang, Adv. Mater. 26 (2014) 4121.
[44] Y. Wang, X. Wang, M. Antonietti, Angew. Chem. Int. Ed. 51 (2012) 68.
[45] W.K. Jo, T.S. Natarajan, J. Colloid Interf. Sci. 482 (2016) 58.
[46] M. Yan, F. Zhu, W. Gu, L. Sun, W. Shi, Y. Hua, RSC Adv. 6 (2016) 61162.
[47] J.L. Gong, B. Wang, G.M. Zeng, C.P. Yang, C.G. Niu, Q.Y. Niu, W.J. Zhou, Y. Liang, J. Hazard. Mater. 164 (2009) 1517.
[48] D.L. Huang, G.M. Zeng, C.L. Feng, S. Hu, X.Y. Jiang, L. Tang, F.F. Su, Y. Zhang, W. Zeng, H.L. Liu, Environ. Sci. Technol. 42 (2008) 4946.
[49] X.J. Hu, J.S. Wang, Y.G. Liu, X. Li, G.M. Zeng, Z.L. Bao, X.X. Zeng, A.W. Chen, F. Long, J. Hazard. Mater. 185 (2011) 306.
[50] Y. Ji, J. Cao, L. Jiang, Y. Zhang, Z. Yi, J. Alloys Compd. 590 (2014) 9.
[51] Y.C. Deng, L. Tang, G.M. Zeng, Z.J. Zhu, M. Yan, Y.Y. Zhou, J.J. Wang, Y.N. Liu, J.J. Wang, Appl. Catal. B: Environ. 203 (2017) 343.
[52] J. Ran, T.Y. Ma, G. Gao, X.-W. Du, S.Z. Qiao, Energy Environ. Sci. 8 (2015) 3708.
[53] J. Yu, A. Kudo, Adv. Funct. Mater. 16 (2006) 2163.
[54] W. Zhao, Y. Liu, Z. Wei, S. Yang, H. He, C. Sun, Appl. Catal. B – Environ. 185 (2016) 242.
[55] Y. Zhou, L. Zhang, W. Huang, Q. Kong, X. Fan, M. Wang, J. Shi, Carbon 99 (2016) 111.
[56] P. Niu, L. Zhang, G. Liu, H.-M. Cheng, Adv. Funct. Mater. 22 (2012) 4763.
[57] N. Tian, H. Huang, Y. He, Y. Guo, T. Zhang, Y. Zhang, Dalton Trans. 44 (2015) 4297.
[58] J. Cao, C. Zhou, H. Lin, B. Xu, S. Chen, Appl. Surf. Sci. 284 (2013) 263.
[59] J. Xu, L. Zhang, R. Shi, Y. Zhu, J. Mater. Chem. A 1 (2013) 14766.
[60] X. She, H. Xu, Y. Xu, J. Yan, J. Xia, L. Xu, Y. Song, Y. Jiang, Q. Zhang, H. Li, J. Mater. Chem. A 2 (2014) 2563.
[61] F. Guo, W. Shi, X. Lin, G. Che, J. Phys. Chem. Solids 75 (2014) 1217.
[62] Z.H. Ai, W.K. Ho, S.C. Lee, L.Z. Zhang, Environ. Sci. Technol. 43 (2009) 4143.
[63] Y. Zhou, L. Zhang, J. Liu, X. Fan, B. Wang, M. Wang, W. Ren, J. Wang, M. Li, J. Shi, J. Mater. Chem. A 3 (2015) 3862.
[64] J. Di, J. Xia, X. Li, M. Ji, H. Xu, Z. Chen, H. Li, Carbon 107 (2016) 1.
[65] F. Chen, Q. Yang, Y. Zhong, H. An, J. Zhao, T. Xie, Q. Xu, X. Li, D. Wang, G. Zeng, Water Res. 101 (2016) 555.
[66] C. Ai, D. Zhou, Q. Wang, X. Shao, Y. Lei, Sol. Energy 113 (2015) 34.
[67] B. Zhou, X. Zhao, H. Liu, J. Qu, C.P. Huang, Appl. Catal. B – Environ. 99 (2010) 214.
[68] Y. Ji, Y. Shi, W. Dong, X. Wen, M. Jiang, J. Lu, Chem. Eng. J. 298 (2016) 225.
[69] D. He, Y. Sun, L. Xin, J. Feng, Chem. Eng. J. 258 (2014) 18.
[70] V. Maroga Mboula, V. Hequet, Y. Gru, R. Colin, Y. Andres, J. Hazard. Mater. 209–210 (2012) 355.